

# The Impact of Group Delay Dispersion on Radar Imaging With Multiresonant Antennas

Jonathan Witte-meier<sup>1</sup>, Benedikt Sievert<sup>1</sup>, *Member, IEEE*, Muhamed Dedic<sup>1</sup>, Daniel Erni<sup>1</sup>, *Member, IEEE*, Andreas Rennings<sup>1</sup>, *Member, IEEE*, and Nils Pohl<sup>1</sup>, *Senior Member, IEEE*

**Abstract**—Radar sensing has become very popular over the last two decades, and research has focused on high-bandwidth and high-resolution systems. Due to the steadily increasing center frequency of front-end circuits, on-chip antennas are the preferred choice over PCB antennas and horn antennas when frequencies get close to THz. However, conventional on-chip antennas are severely limited in bandwidth, leading to increased use of wideband and multiresonant on-chip antennas. Besides a more complex design process of multiresonant antennas, they have the disadvantage of a nonconstant dispersive group delay (GD). This reduces the resolution of sensing systems, such as the range resolution and angular resolution of a radar system. In this work, we show how GD affects the imaging properties of a radar system. The measured S-parameter data from a 240-GHz multiresonant antenna are used to generate synthetic intermediate frequency (IF) signals of a rectangular array. Subsequently, simulated 3-D radar images are generated using the backprojection algorithm. These images are compared with those of a nondispersive imaging system. Finally, two compensation methods using a phase correction method and an all-pass filter are explained, and their performance is compared.

**Index Terms**—Antennas theory and design, array, B11HFC, dispersion, group delay (GD), millimeter wave (mmWave), multiresonant, patch antenna, radar imaging, silicon-germanium (SiGe)/Si technologies, terahertz (THz).

## I. INTRODUCTION

A KEY component of millimeter-wave (mm-wave) and THz sensing is the antenna used to transmit the front-end signal into free-space [1]. While voltage-controlled oscillators can offer over 30% relative tuning range in the mm-wave spectrum [2], the system's resolution is often limited to the antenna's bandwidth when using on-chip antennas [3]. While digital postprocessing can compensate for the narrowband properties of on-chip antennas, it can increase the noise floor [4], [5]. In general, the metal stack of MMICs is not suitable to realize broadband antennas. This is due to the small distance between the top metal layer (patch) and the

bottom metal layer (ground plane), which leads to reduced efficiency at the front-side radiation [6] and a reduced gain [7], [8]. The solutions to increase efficiency are manifold and range from the off-chip ground [9], dielectric resonators [10]–[12], nonplanar antennas [13], [14], and backside radiation techniques [15].

In this letter, we analyze a circular-polarized multiresonant antenna with an on-chip ground plane. Multiple resonant structures increase bandwidth and series capacitive elements enhance the radiation efficiency (similar to [16]). This has the advantage that no complex and additional manufacturing processes are necessary as with the previously mentioned approaches. The impact of the antenna's group delay (GD) on the image quality is analyzed while excluding the antenna's gain to separate one imperfection from the other.

GD analysis of antennas has been studied in other areas, such as ultrawideband antennas for communication systems [17]–[20] and GPS applications [21]–[24]. Usual radar calibration methods utilize reference measurements of targets to characterize and compensate for the phase and amplitude imperfections in single-channel [4], [5] and multiple-input and multiple-output (MIMO) radar systems, where phase differences and mutual coupling between antennas become important [25]–[33].

In the following, the system model, including algorithms (see Section II), the antenna including measurement and simulation results (see Section III), and the imaging results (see Section IV), is shown in detail, followed by a conclusion in Section V.

## II. SYSTEM MODEL FOR AN FMCW MIMO RADAR

The system model is based on an FMCW radar system with one transmit and 16 receive antennas (SIMO), which corresponds to two orthogonal uniform line arrays with four transmit and receive antennas (MIMO), respectively. The antennas are placed equally with a distance of  $0.5\lambda_c$ . The center frequency is 240-GHz, and the bandwidth is 40 GHz, which corresponds to a relative bandwidth of 16.6%. The system parameters and antenna setup are shown in Table I and Fig. 1, respectively. The complex intermediate frequency (IF) signal is modeled by

$$s_{\text{IF}}^c(\mathbf{m}_{\text{Tx}}, \mathbf{m}_{\text{Rx}}, \mathbf{m}_k) = \sum_{i=1}^P \mathbf{w}_A(\mathbf{m}_{\text{Tx}}, \mathbf{m}_{\text{Rx}}, \mathbf{r}_i) \times e^{-j\mathbf{k}_r \cdot (|\mathbf{r}_i - \mathbf{r}_{\text{Tx}}| + |\mathbf{r}_i - \mathbf{r}_{\text{Rx}}|)} + \mathbf{N} \quad (1)$$

Manuscript received September 1, 2021; revised October 25, 2021; accepted November 3, 2021. Date of publication December 3, 2021; date of current version March 11, 2022. This work was supported by the German Research Foundation [Deutsche Forschungsgemeinschaft (DFG)] under Project 287022738 TRR 196 for Project C03 and C05. (Corresponding author: Jonathan Witte-meier.)

Jonathan Witte-meier and Nils Pohl are with the Institute of Integrated Systems, Ruhr University Bochum, 44801 Bochum, Germany (e-mail: jonathan.witte-meier@rub.de).

Benedikt Sievert, Muhamed Dedic, Daniel Erni, and Andreas Rennings are with the Department of General and Theoretical Electrical Engineering (ATE), University of Duisburg-Essen, 47048 Duisburg, Germany.

Color versions of one or more figures in this letter are available at <https://doi.org/10.1109/LMWC.2021.3128281>.

Digital Object Identifier 10.1109/LMWC.2021.3128281

TABLE I  
SYSTEM PARAMETERS

Name	Symbol	Value
Center frequency	$f_c$	240 GHz
Bandwidth	$B$	40 GHz
Maximum range	$r_{\max}$	3.84 m
Chirp duration	$T$	2048 $\mu$ s
Sampling frequency	$f_s$	1 MHz
Number of frequency points	$M_k$	2048
Number of Tx antennas	$M_{\text{Tx}}$	1
Number of Rx antennas	$M_{\text{Rx}}$	16
x/y spacing of Rx antennas	$d_{\text{Rx}}$	$0.5 \lambda_c$
Signal-to-noise ratio	SNR	20 dB
Number of voxel in x/y/z direction	$N_x, N_y, N_z$	4096
Voxel size	$d_{\text{vox}}$	468.43 $\mu$ m

where  $P$  is the number of targets at  $\mathbf{r}_i$ ,  $\mathbf{w}_A$  is the combined radiation characteristic of the  $m_{\text{Tx}}$ -th transmit antenna (located at  $\mathbf{r}_{\text{Tx}}$ ) and the  $m_{\text{Rx}}$ -th receive antenna (located at  $\mathbf{r}_{\text{Rx}}$ ), and  $\mathbf{N}$  is the additive white Gaussian noise. The discrete wavenumber of the sampled IF signal ( $f_s = 1/T_s$ ) is given by

$$\mathbf{k}_r = \frac{2\pi f_c}{c_0} + \mathbf{m}_k \frac{2\pi B T_s}{c_0 T} \quad (2)$$

where the steps are given by  $\mathbf{m}_k = -(M_k/2), \dots, (M_k/2) - 1$ .

#### A. Back-Projection Algorithm

The 3-D radar image is calculated with the backprojection algorithm [34]. Here, the voxel's amplitude at positions  $(n_x, n_y, n_z)$  is given by

$$A[n_x, n_y, n_z] = \sum_{m_{\text{Tx}}} \sum_{m_{\text{Rx}}} \sum_{m_k} \mathbf{x}_{\text{IF}}^c[m_{\text{Tx}}, m_{\text{Rx}}, m_k] \cdot \mathbf{s}_{\text{IF},0}^*[m_{\text{Tx}}, m_{\text{Rx}}, m_k] \Big|_{\mathbf{r}_0[n_x, n_y, n_z]} \quad (3)$$

where  $\mathbf{s}_{\text{IF},0}^*$  is the ideal IF signal ( $\mathbf{w}_A = \mathbf{1}$  and no noise) of a point target at  $\mathbf{r}_0$  and  $\mathbf{x}_{\text{IF}}^c$  is the synthetic IF signal based on (1). To ensure a fast calculation, the calculation is accelerated with an inverse fast Fourier transformation [35].

### III. ANTENNA MEASUREMENTS AND SIMULATION RESULTS

The investigated antenna utilizes the on-chip ground-plane provided by the B11HFC silicon-germanium (SiGe) metal stack from Infineon Technologies AG. It radiates a circular polarization (CP) into broadside direction over a bandwidth covering roughly 220–260 GHz, where the axial ratio of the CP declines for both directions off broadside and frequencies at the edges of the bandwidth. The differential feeding of the antenna is provided by the balun connected to the probing pads [cf. Fig. 1(b) and (c)].

To characterize the angle-dependent GD of the on-chip antenna, the spherical measurement system from [36] is used. Since the GD characterization is very sensitive to even minor multipath contributions and system calibration drift [21], a waveguide-based two-port calibration assured the compensation of any GD inherent to the vector network analyzer and the utilized frequency extenders. Furthermore, the error-two-port of the utilized on-chip probe was measured by on-wafer calibration standards to compensate for its additional GD. Finally,

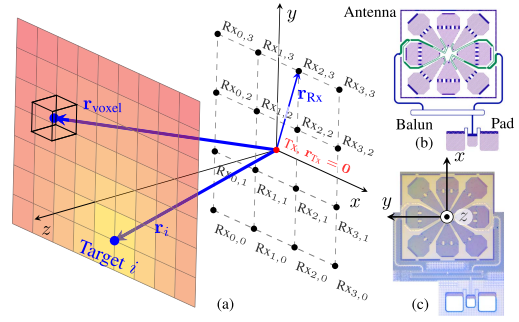


Fig. 1. Antenna arrangement at (a)  $z = 0$  plane and  $xy$  image plane; (b) top view on the simulated antenna, balun, and pads and (c) realized one.

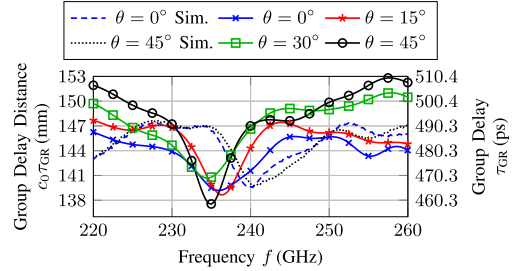


Fig. 2. Measured and simulated GD for different elevation angles  $\theta$  at  $\varphi = 0^\circ$ .

the GD was measured with an open-ended waveguide acting as a receive antenna, which was placed at a distance of about 140 mm from the on-chip antenna radiating into free space.

The measurement method used here is similar to [37]. To reduce the disturbing effect of multipath, both the on-chip probe and the receiving waveguide flange were covered in mm-wave absorbers, and the receiver mismatch was compensated by a 15-dB attenuator, as described in [21]. Also, first-order reflections reverse the CP from RHCP to LHCP. Therefore, the contribution of probe reflections to the GD measurement is reduced. Finally, the GD shown in Fig. 2 was obtained by superimposing the transmission coefficients of two orthogonal polarizations

$$S_{21,\text{RHCP}} = \frac{S_{21,\theta} - j S_{21,\varphi}}{\sqrt{2}} \quad (4)$$

and time-gating the calculated  $S_{21,\text{RHCP}}$  with a hamming window of 288-ps length. Generally, the measured and simulated GDs are very comparable for different elevation angles  $\theta$ , and however, a frequency shift of 5 GHz between simulation and measurement can be observed.

#### A. GD Modeling

The GD is determined via the partial derivative of the phase of  $S_{21}$  with respect to the frequency [38, p. 64]

$$\tau_{\text{GD}} = -\frac{\partial \phi(S_{21})}{2\pi \cdot \partial f} \quad (5)$$

The measured and direction-dependent GDs (see Fig. 2) are added to the synthetic IF signal [see (1)] using

$$\mathbf{x}_{\text{IF,GD}}^c[m_{\text{Tx}}, m_{\text{Rx}}, m_k] = \sum_{i=1}^P \mathbf{s}_{\text{IF}}^c[m_{\text{Tx}}, m_{\text{Rx}}, m_k] \cdot e^{j\phi(S_{21,\text{Tx},i})} \cdot e^{j\phi(S_{21,\text{Rx},i})} \quad (6)$$

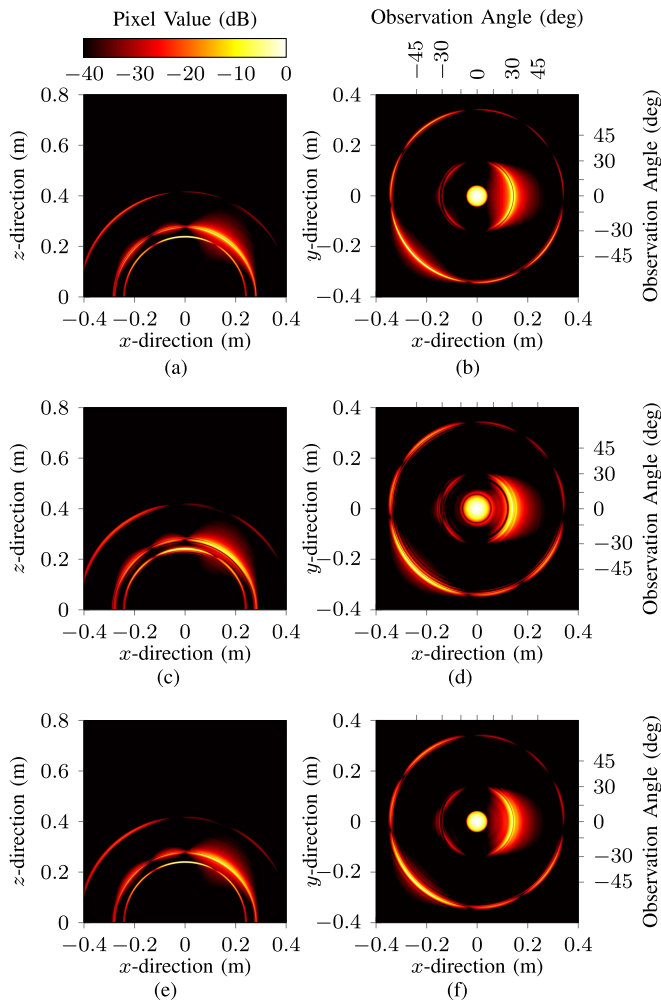


Fig. 3. Radar images along a horizontal cross section (left) and cross range (right) without, with, and with compensated GD. (a)  $xz$  plane (ideal). (b)  $xy$  plane (ideal). (c)  $xz$  plane (with GD). (d)  $xy$  plane (with GD). (e)  $xz$  plane (with GD and all-pass compensation). (f)  $xy$  plane (with GD and all-pass compensation).

where  $\phi(S_{21,Tx,i})$  and  $\phi(S_{21,Rx,i})$  contain the angle-dependent phase of the  $S$ -parameter of target  $i$ .

### B. Phase Correction

In (6), the impact of the GD is modeled by multiplying an exponential term to the ideal IF signal. To compensate for the GD, the simulation data of the GD is multiplied to the disturbed IF signal using

$$\hat{\mathbf{x}}_{\text{IF,GD}}^c[m_{\text{Tx}}, m_{\text{Rx}}, m_k] = \mathbf{x}_{\text{IF,GD}}^c[m_{\text{Tx}}, m_{\text{Rx}}, m_k] \cdot e^{-2j\phi(S_{21,B})} \quad (7)$$

where  $\phi(S_{21,B})$  contains the phase of the  $S_{21}$   $S$ -parameter in broadside direction. The method is very similar to the Hilbert-transform-based method presented in [4].

### C. All-Pass Filter

All-pass filters compensate for the delay of different frequency components while maintaining a constant amplitude [39]. Here, MATLAB's DSP System Toolbox with the

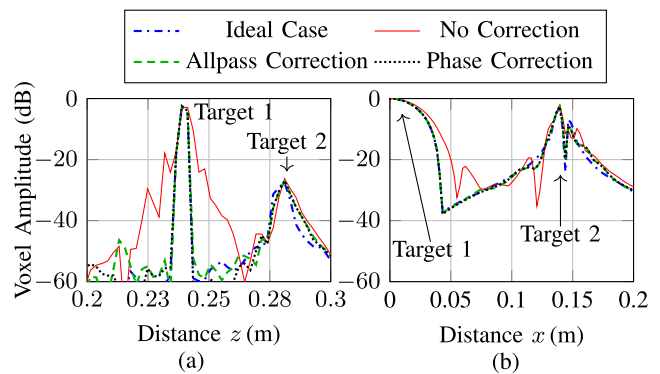


Fig. 4. Spectrum in (a) range and (b) cross-range direction. (a)  $z$ -axis for  $x = 0$  and  $y = 0$ . (b)  $x$ -axis for  $y = 0$  and  $z = z_{\text{Target}}$ .

arbitrary GD filter is used, which utilizes an iterative optimization procedure to enhance the phase response error [40]. The general form of an all-pass filter is given by

$$H_{\text{ap}}(z) = \prod_{k=1}^M \frac{z^{-1} - d_k}{1 - d_k z^{-1}} \prod_{k=1}^N \frac{(z^{-1} - c_k)(z^{-1} - c_k^*)}{(1 - c_k z^{-1})(1 - c_k^* z^{-1})} \quad (8)$$

where  $d_k$  and  $c_k$  denote the real- and complex-valued poles, respectively. The input of the all-pass filter is the Fourier transform of (6). Hereby, the sample points of the IF signal will be shifted with respect to the corresponding RF signal. The all-pass filter will delay the IF frequency components and increase the target's distance proportional to the filter order of 14, which can be compensated using a shift operation.

## IV. IMAGING RESULTS

In this section, the effect of the GD with radar images is shown. Here, three point targets at  $(\theta, \phi) = (0^\circ, 0^\circ)$ ,  $(30^\circ, 0^\circ)$ , and  $(-45^\circ, -45^\circ)$  are used, and cut planes are shown. Fig. 3(a) and 3(b) show the ideal case with a constant GD and an ideal antenna gain ( $\mathbf{w}_A = \mathbf{1}$ ). In Fig. 3(c) and 3(d), the GD is added and the pulses are spread. Fig. 3(e) and (f) shows the corrected radar images by using an all-pass filter. Hereby, the image quality is improved significantly. The radar images of the phase correction method [see (7)] are practically indistinguishable from the all-pass results (see Fig. 4). Fig. 4 shows the cutting line at  $x = y = 0$  in (a) and at  $y = 0$ ,  $z = z_{\text{target}}$  in (b). The GD spreads the  $-6$ - and  $-20$ -dB pulsewidth from 3.74 and 6.23 mm to 4.11 and 10.72 mm, respectively. With both correction methods, this can be compensated so that the ideal case is almost achieved.

## V. CONCLUSION

In this letter, we showed how the GD of a multiresonant, circularly polarized on-chip antenna affects the imaging quality. On the one hand, the GD generates sidelobes, and on the other hand, it spreads the main lobes. The correction methods presented include a phase correction term and filtering with an all-pass, both applied directly to the IF signal. Significant improvements are obtained with both procedures, even though the correction is performed with the broadside GD data. For imaging far off broadside direction, an angle-dependent GD compensation should be applied in the backprojection algorithm.

## REFERENCES

- [1] P. Hillger *et al.*, "Toward mobile integrated electronic systems at THz frequencies," *J. Infr. Millim. THz Waves*, vol. 41, no. 7, pp. 846–869, 2020.
- [2] C. Bredendiek, K. Aufinger, and N. Pohl, "Full waveguide E- and W-band fundamental VCOs in SiGe:C technology for next generation FMCW radars sensors," in *Proc. 14th Eur. Microw. Integr. Circuits Conf. (EuMIC)*, Paris, France, Sep. 2019, pp. 148–151.
- [3] T. Jaeschke, C. Bredendiek, and N. Pohl, "A 240 GHz ultra-wideband FMCW radar system with on-chip antennas for high resolution radar imaging," in *IEEE MTT-S Int. Microw. Symp. Dig.*, Jun. 2013, pp. 1–4.
- [4] S. Thomas, C. Bredendiek, and N. Pohl, "A SiGe-based 240-GHz FMCW radar system for high-resolution measurements," *IEEE Trans. Microw. Theory Techn.*, vol. 67, no. 11, pp. 4599–4609, Nov. 2019.
- [5] S. Thomas, A. Froehly, C. Bredendiek, R. Herschel, and N. Pohl, "High resolution SAR imaging using a 240 GHz FMCW radar system with integrated on-chip antennas," in *Proc. 15th Eur. Conf. Antennas Propag. (EuCAP)*, Dusseldorf, Germany, Mar. 2021, pp. 1–5.
- [6] T. Hirano, K. Okada, J. Hirokawa, and M. Ando, "60 GHz on-chip patch antenna integrated in a 0.18- $\mu\text{m}$  CMOS technology," in *Proc. Int. Symp. Antennas Propag. (ISAP)*, Nagoya, Japan, 2012, pp. 62–65.
- [7] R. Han *et al.*, "A 280-GHz Schottky diode detector in 130-nm digital CMOS," *IEEE J. Solid-State Circuits*, vol. 46, no. 11, pp. 2602–2612, Nov. 2011.
- [8] Z. Chen, C.-C. Wang, H.-C. Yao, and P. Heydari, "A BiCMOS W-band  $2 \times 2$  focal-plane array with on-chip antenna," *IEEE J. Solid-State Circuits*, vol. 47, no. 10, pp. 2355–2371, Oct. 2012.
- [9] T. Zwick, D. Liu, and B. P. Gaucher, "Broadband planar superstrate antenna for integrated millimeterwave transceivers," *IEEE Trans. Antennas Propag.*, vol. 54, no. 10, pp. 2790–2796, Oct. 2006.
- [10] D. L. Cuenca, J. Hesselbarth, and G. Alavi, "Chip-mounted dielectric resonator antenna with alignment and testing features," in *Proc. 46th Eur. Microw. Conf. (EuMC)*, London, U.K., pp. 723–726.
- [11] B. Sievert, J.-T. Svejda, D. Erni, and A. Rennings, "Mutually coupled dielectric resonators for on-chip antenna efficiency enhancement," in *Proc. 2nd Int. Workshop Mobile THz Syst. (IWMTS)*, Bad Neuenahr, Germany, 2019, pp. 1–4.
- [12] C.-H. Li and T.-Y. Chiu, "340-GHz low-cost and high-gain on-chip higher order mode dielectric resonator antenna for THz applications," *IEEE Trans. THz Sci. Technol.*, vol. 7, no. 3, pp. 284–294, May 2017.
- [13] P. Stärke, D. Fritsche, S. Schumann, C. Carta, and F. Ellinger, "High-efficiency wideband 3-D on-chip antennas for subterahertz applications demonstrated at 200 GHz," *IEEE Trans. THz Sci. Technol.*, vol. 7, no. 4, pp. 415–423, Jul. 2017.
- [14] X.-D. Deng, Y. Li, C. Liu, W. Wu, and Y.-Z. Xiong, "340 GHz on-chip 3-D antenna with 10 dBi gain and 80% radiation efficiency," *IEEE Trans. THz Sci. Technol.*, vol. 5, no. 4, pp. 619–627, Jul. 2015.
- [15] J. Grzyb, K. Statnikov, N. Sarmah, B. Heinemann, and U. R. Pfeiffer, "A 210–270-GHz circularly polarized FMCW radar with a single-lens-coupled SiGe HBT chip," *IEEE Trans. THz Sci. Technol.*, vol. 6, no. 6, pp. 771–783, Nov. 2016.
- [16] B. Sievert, J. T. Svejda, J. Wittemeier, N. Pohl, D. Erni, and A. Rennings, "Equivalent circuit model separating dissipative and radiative losses for the systematic design of efficient microstrip-based on-chip antennas," *IEEE Trans. Microw. Theory Techn.*, vol. 69, no. 2, pp. 1282–1294, Feb. 2021.
- [17] D.-H. Kwon, "Effect of antenna gain and group delay variations on pulse-preserving capabilities of ultrawideband antennas," *IEEE Trans. Antennas Propag.*, vol. 54, no. 8, pp. 2208–2215, Aug. 2006.
- [18] P. McEvoy, M. John, S. Curto, and M. J. Ammann, "Group delay performance of ultra wideband monopole antennas for communication applications," in *Proc. Loughborough Antennas Propag. Conf.*, Loughborough, U.K., Mar. 2008, pp. 377–380.
- [19] M. N. Hasan and M. Seo, "A planar 3.4–9 GHz UWB monopole antenna," in *Proc. Int. Symp. Antennas Propag. (ISAP)*, Busan, South Korea, 2018, pp. 1–2.
- [20] N. Anveshkumar and A. S. Gandhi, "Design and performance analysis of a modified circular planar monopole UWB antenna," in *Proc. 8th Int. Conf. Comput., Commun. Netw. Technol. (ICCCNT)*, Delhi, India, Jul. 2017, pp. 1–5.
- [21] P. Miller, "The measurement of antenna group delay," in *Proc. 8th Eur. Conf. Antennas Propag. (EuCAP)*, The Hague, The Netherlands, Apr. 2014, pp. 1488–1492.
- [22] H. Lin, Z. Song, X. Wang, and H. Gao, "An antenna group delay measurement method based on three-antenna extrapolation and least residual error curve fitting technique," *Microw. Opt. Technol. Lett.*, vol. 60, no. 7, pp. 1608–1612, Jul. 2018.
- [23] A. Raghuvanshi and F. van Graas, "Impact of antenna group delay variations on protection levels," in *Proc. IEEE/ION Position, Location Navigat. Symp. (PLANS)*, Savannah, GA, USA, Apr. 2016, pp. 857–862.
- [24] H. Lin, Z. Song, X. Wang, and H. Gao, "An improved antenna group delay measurement method using a three-antenna extrapolation technique," *Radioengineering*, vol. 26, no. 3, pp. 675–681, Sep. 2017.
- [25] A. Figueroa, N. Joram, and F. Ellinger, "Automatic delay and phase mismatch calibration in FMCW MIMO radar," in *Proc. 17th Eur. Radar Conf. (EuRAD)*, Utrecht, The Netherlands, 2020, pp. 402–405.
- [26] C. M. Schmid, C. Pfeffer, R. Feger, and A. Stelzer, "An FMCW MIMO radar calibration and mutual coupling compensation approach," in *Proc. Eur. Radar Conf.*, Nuremberg, Germany, 2013, pp. 13–16.
- [27] G. Korner, D. Oppelt, J. Adametz, and M. Vossiek, "Novel passive calibration method for fully polarimetric near field MIMO imaging radars," in *Proc. 12th German Microw. Conf. (GeMiC)*, Stuttgart, Germany, Mar. 2019, pp. 150–153.
- [28] Y. Z. Liu, X. Xu, and G. Xu, "MIMO radar calibration and imagery for near-field scattering diagnosis," *IEEE Trans. Aerosp. Electron. Syst.*, vol. 54, no. 1, pp. 442–452, Feb. 2018.
- [29] M. Harter, J. Hildebrandt, A. Ziroff, and T. Zwick, "Self-calibration of a 3-D-digital beamforming radar system for automotive applications with installation behind automotive covers," *IEEE Trans. Microw. Theory Techn.*, vol. 64, no. 9, pp. 2994–3000, Sep. 2016.
- [30] S. Vakalis, L. Gong, Y. He, J. Papapolymerou, and J. A. Nanzer, "Experimental demonstration and calibration of a 16-element active incoherent millimeter-wave imaging array," *IEEE Trans. Microw. Theory Techn.*, vol. 68, no. 9, pp. 3804–3813, Sep. 2020.
- [31] A. Dürr, M. Linder, and C. Waldschmidt, "Increasing the efficiency and robustness of angular radar calibration by exploiting phase symmetry," in *Proc. 17th Eur. Radar Conf. (EuRAD)*, Utrecht, The Netherlands, 2021, pp. 30–33.
- [32] C. Vasanelli *et al.*, "Calibration and direction-of-arrival estimation of millimeter-wave radars: A practical introduction," *IEEE Antennas Propag. Mag.*, vol. 62, no. 6, pp. 34–45, Dec. 2020.
- [33] A. Dürr, R. Kramer, D. Schwarz, M. Geiger, and C. Waldschmidt, "Calibration-based phase coherence of incoherent and quasi-coherent 160-GHz MIMO radars," *IEEE Trans. Microw. Theory Techn.*, vol. 68, no. 7, pp. 2768–2778, Jul. 2020.
- [34] A. Haderer, P. Scherz, J. Schrattecker, and A. Stelzer, "Real-time implementation of an FMCW backprojection algorithm for 1D and 2D apertures," in *Proc. 8th Eur. Radar Conf.*, Manchester, U.K., 2011, pp. 53–56.
- [35] L. M. H. Ulander, H. Hellsten, and G. Stenström, "Synthetic-aperture radar processing using fast factorized back-projection," *IEEE Trans. Aerosp. Electron. Syst.*, vol. 39, no. 3, pp. 760–776, Jul. 2003.
- [36] B. Sievert, J. T. Svejda, D. Erni, and A. Rennings, "Spherical mm-wave/THz antenna measurement system," *IEEE Access*, vol. 8, pp. 89680–89691, 2020.
- [37] M. D. Blech, S. Koch, and S. Saito, "Rectangular waveguide based polarizer for mm-wave antenna measurements," in *Proc. 6th Eur. Conf. Antennas Propag. (EuCAP)*, Mar. 2012, pp. 3487–3490.
- [38] R. E. Ziemer and W. H. Tranter, *Principles of Communications*, 7th ed. Hoboken, NJ, USA: Wiley, 2015.
- [39] M. Lang, "Allpass filter design and applications," *IEEE Trans. Signal Process.*, vol. 46, no. 9, pp. 2505–2514, Sep. 1998.
- [40] A. Antoniou, *Digital Signal Processing*. New York, NY, USA: McGraw-Hill, 2006.